

# Few-Layer Ag-Coated Ordered Mesoporous Pt Nanocrystals for Ethanol Oxidation

Xian Wang, Zhe Zhang, Yongjie Ge,\* Kui Shen, and Jinjie Qian\*

Direct ethanol fuel cells have broad application prospects, but there are still some issues such as slow oxidation kinetics and poisoning effects of intermediates in the anodic ethanol reduction reaction (EOR). Herein, a series of few-layer Ag-coated ordered mesoporous Pt nanocrystals (Meso-Pt@Ag) with different Ag shell thicknesses are prepared by combining hard templating and in situ reduction methods. Benefiting from the ordered mesoporous structure, the lattice strain, and the electronic synergistic effect induced by the core-shell structure, Meso-Pt@Ag<sub>2</sub> nanocrystals exhibit the best EOR performance with a mass activity of 10.01 A mg<sub>Pt</sub><sup>-1</sup>, which is 8.40-fold of commercial Pt/C and 4.45-fold of Meso-Pt, respectively. And, Meso-Pt@Ag<sub>2</sub> nanocrystals also show the favorable toxicity resistance to carbonaceous intermediates and stability for EOR. Furthermore, theoretical calculations demonstrate that the Ag-coated Pt core has more optimized deprotonation reaction kinetics and lower CO adsorption energy, indicating its better resistance to CO toxicity for EOR.

On the other hand, DEFCs exhibit higher theoretical energy density than direct methanol or formic acid fuel cells.<sup>[9]</sup> In principle, there are two main reaction pathways in the anodic ethanol oxidation reaction (EOR): the C<sub>2</sub> pathway of 4-electron transfer for incomplete oxidation of ethanol to acetic acid or acetate; and the C<sub>1</sub> pathway of 12-electron transfer for complete oxidation to CO<sub>2</sub>.<sup>[10,11]</sup> During EOR, the slow alcohol oxidation kinetics and the poisoning effect of CO-like carbonaceous intermediates severely limit the reaction efficiency of catalysts.<sup>[9]</sup> At present, Pt- and Pd-based catalysts endow with highly efficient catalytic activity for EOR, but the scarcity of noble metals and some challenges in stability hinder their large-scale industrial applications.<sup>[12,13]</sup> Therefore, the rational modification of Pt or Pd metals with other

cheaper metals can improve the EOR performance of catalysts, reduce the use of noble metals, and alleviate the scarcity of noble metals.<sup>[14]</sup>

Generally, core-shell structured particles exhibit better electrocatalytic performance compared with single-phase components, and thus have been widely studied.<sup>[15,16]</sup> A variety of core-shell nanoparticles can be obtained by adjusting their core and shell layers.<sup>[17,18]</sup> The interesting electronic interactions between the core and shell bring in three special effects, including bulk effect,<sup>[19]</sup> ligand effect,<sup>[20]</sup> and geometric effect,<sup>[21]</sup> which can be used to improve the electrocatalytic performance of the catalysts. Previously, Huang et al. synthesized hexagonal PtPb/Pt core-shell structured nanoplates,<sup>[22]</sup> in which the unique biaxial strain occurs between the few-layer Pt shell and the PtPb alloy core, enabling some Pt atoms on the surface to show the optimized Pt-O adsorption energy, thereby greatly enhancing their oxygen reduction activity. Metal Ag owns excellent electron transfer ability, structural stability, and high electrical conductivity, and is usually alloyed with Pt to facilitate its EOR performance by tuning the *d*-band center of Pt down through the synergistic effect of electronic structure and the lattice strain of the PtAg alloy.<sup>[23]</sup> Due to the Kirkendall effect, the growth of Pt shells based on Ag cores is likely to destroy the original Ag cores so that the Pt@Ag core-shell structure cannot be conveniently formed. Therefore, we expect to improve the EOR activity by changing the electronic structure of the Ag shell through the Pt@Ag core-shell structure formed by wrapping Ag on the Pt core. In particular, the electronic effects and lattice strain of the core-shell structure become more prominent as the shell thickness decreases.<sup>[24]</sup> The smaller lattice spacing of Pt will cause a

## 1. Introduction

With the rapid development of society, there is an urgent need for researchers to develop advanced energy storage devices to meet the ever-growing demand for energy.<sup>[1–3]</sup> Since the 1950s, proton exchange membrane fuel cells have attracted extensive attention on account of their high power density, high energy density, high energy conversion efficiency, clean products, etc.<sup>[4,5]</sup> Among them, direct ethanol fuel cells (DEFCs) have bright application prospects.<sup>[6,7]</sup> On the one hand, compared with other gaseous fuels such as H<sub>2</sub>, CH<sub>4</sub>, and CO, ethanol owns the advantages of low toxicity, easy storage, and abundant sources.<sup>[8]</sup>

X. Wang, Z. Zhang, Y. Ge, J. Qian  
College of Chemistry and Materials Engineering  
Wenzhou University  
Wenzhou 325000, P. R. China  
E-mail: geyongjie1220@wzu.edu.cn; jinjieqian@wzu.edu.cn

X. Wang, K. Shen  
Laboratory of Fuel Cell Technology of Guangdong Province  
School of Chemistry and Chemical Engineering  
South China University of Technology  
Guangzhou 510640, P. R. China

 The ORCID identification number(s) for the author(s) of this article can be found under <https://doi.org/10.1002/ssstr.202200390>.

© 2023 The Authors. Small Structures published by Wiley-VCH GmbH. This is an open access article under the terms of the Creative Commons Attribution License, which permits use, distribution and reproduction in any medium, provided the original work is properly cited.

DOI: 10.1002/ssstr.202200390

certain compressive strain on the Ag shell and change the electronic structure of the surface Ag atoms.<sup>[25]</sup> From this point of view, the rationally designed and regulated core-shell structure of Pt@Ag can make full use of the electronic interaction and lattice strain effects, and will definitely endow the Ag shell with an optimized electronic structure to significantly improve EOR.

Here, we have utilized a strategy combining hard templating and in situ reduction methods to synthesize a series of few-layer Ag-coated ordered mesoporous Pt nanocrystals (Meso-Pt@Ag). By adjusting the thickness of the Ag shell of the core-shell PtAg, the lattice strain and electronic structure of the surface Ag atoms are optimized, thereby realizing the improved EOR performance. Among them, the obtained Meso-Pt@Ag<sub>2</sub> owns a suitable thickness of Ag shell, which enables it to have the optimal lattice strain and electronic structure, thus exhibiting the best EOR performance. Meanwhile, benefiting from the ordered mesoporous structure, Meso-Pt@Ag<sub>2</sub> nanocrystals have fast mass transfer channels, high specific surface area, and abundant catalytic sites, which are favorable for electrocatalytic EOR. Impressively, it achieves the highest mass activity of 10.01 A mg<sub>Pt</sub><sup>-1</sup>, which is 8.40 and 4.45 times higher than those of commercial Pt/C and pure Meso-Pt, and has the favorable antitoxicity and stability for EOR. At last, theoretical calculations further verify that the two-layered Ag-wrapped Pt core has more optimized deprotonation reaction kinetics and lower CO adsorption energy, reflecting its better CO antitoxicity.

## 2. Result and Discussion

### 2.1. Synthesis of Core-Shell Meso-Pt@Ag Nanocrystals

Core-shell Meso-Pt@Ag nanocrystals are first synthesized by the following templating method as depicted in **Figure 1**. The typical molecular sieve KIT-6 with Ia $\bar{3}d$  symmetry exhibits an ordered mesoporous structure with a pore diameter of about 7.9 nm and a high Brunauer-Emmett-Teller (BET)-specific surface area of 636.5 g m<sup>-2</sup> (Figure S1, Supporting Information). Benefiting

from its large porosity and mesopore structure, KIT-6 is rationally chosen as the appropriate hard template. Then, after loading K<sub>2</sub>PtCl<sub>4</sub> into the KIT-6 powder, the ascorbic acid (AA) solution is slowly dropped to reduce Pt ions that uniformly nucleate into a mesoporous template by the classic nanocasting method.<sup>[26]</sup> After the complete Pt crystallization for 12 h, the obtained mesoporous Pt nanocrystals in KIT-6 (Meso-Pt@KIT-6) are conveniently etched with hydrofluoric acid solution to give the black mesoporous Pt nanocrystals (Meso-Pt). Then, the high-purity hydrogen is further bubbled into the suspension of Meso-Pt nanocrystals, in which the highly active surface of Meso-Pt can easily activate H<sub>2</sub> molecules into discrete H atoms as metal hydride of PtH<sub>x</sub> shell, and store the activated H atoms, thus generating the core-shell Meso-Pt@PtH<sub>x</sub>. In this case, these activated H atoms in PtH<sub>x</sub> shell show a strong reductive ability to in situ reduce Ag ions into metal Ag.<sup>[27]</sup> Therefore, AgNO<sub>3</sub> solution is tardily injected into the violently stirred suspension of Meso-Pt@PtH<sub>x</sub> composite to uniformly grow the Ag shell onto the Pt core. As we know, platinum (0.847 V) has a more positive redox potential than silver (0.799 V). Thus, in this process, Ag<sup>+</sup> ions cannot be reduced by Pt atoms, but can only be reduced by active H atoms, which are wrapped in the outer layer of the Pt core to form the Ag shell. By tuning the concentration of AgNO<sub>3</sub> solution, a series of Meso-Pt@Ag with different thicknesses can be easily achieved.

### 2.2. Characterization of Morphology and Structure

Scanning electron microscopy (SEM) and transmission electron microscopy (TEM) images show that monodisperse Meso-Pt@Ag<sub>2</sub> nanocrystals give an average diameter of 80 nm (**Figure 2a-c**, **Figure S2**, Supporting Information). TEM images further reveal that it possesses abundant ordered mesopores, and the growth of the Ag shell does not block the mesopores of Meso-Pt core (**Figure 2c-f**). In **Figure 2e**, two typical nanocrystals observed along the mesoscopic (100) and (111) directions show that the whole core-shell Meso-Pt@Ag<sub>2</sub> is featured with

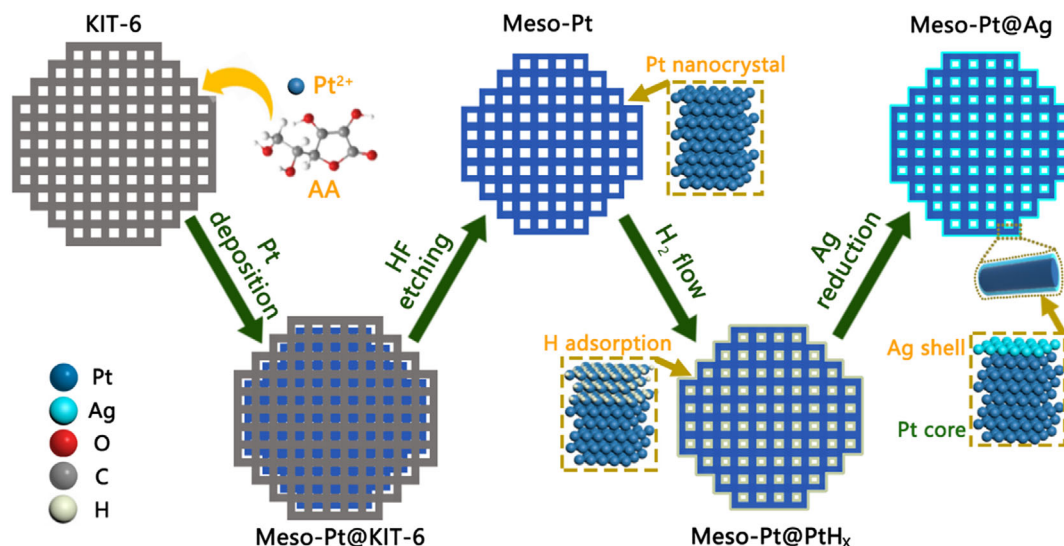


**Figure 1.** Schematic stepwise synthesis of core-shell Meso-Pt@Ag nanocrystals.

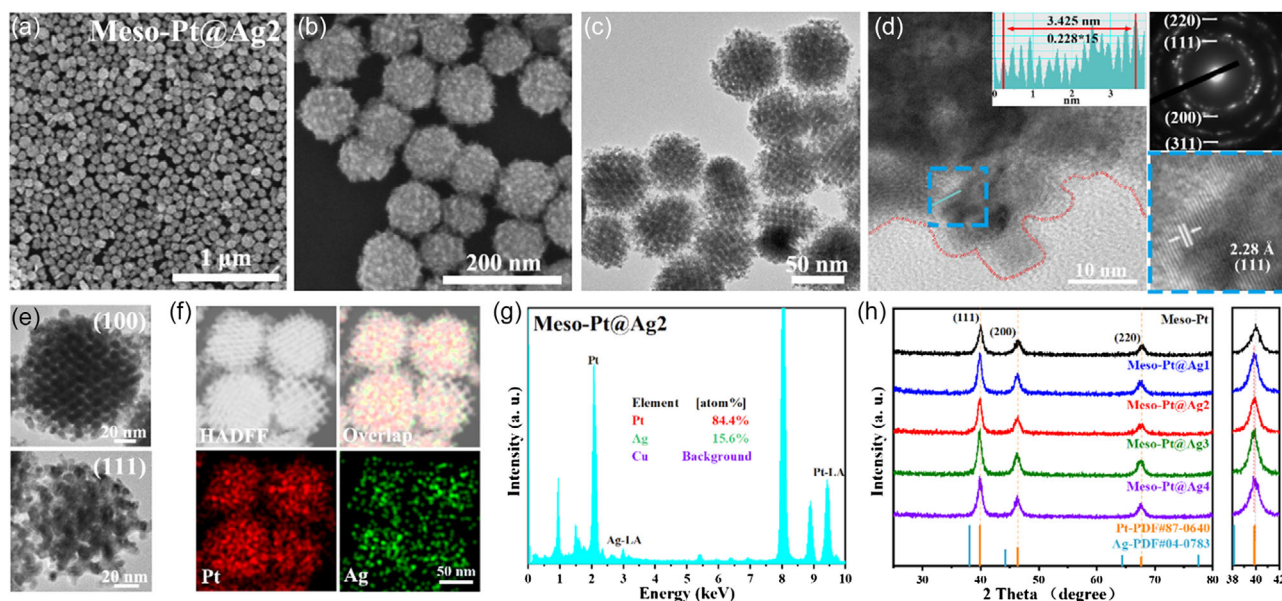


**Figure 2.** Morphology and structure characterizations of Meso-Pt@Ag series. a,b) SEM images, c,e) TEM images, (d) HRTEM and SAED images of Meso-Pt@Ag<sub>2</sub>; e) TEM images along the (100) and (111) directions; f) HAADF-STEM, the corresponding elemental mapping images of Pt and Ag elements, and g) EDS spectrum of the selected Meso-Pt@Ag<sub>2</sub> nanocrystals; h) XRD patterns of Meso-Pt and Meso-Pt@Ag series.

interconnected mesostructures with typical  $Ia\bar{3}d$  symmetry.<sup>[28]</sup> It verifies that the mesoporous Pt core has been completely nanocast from the KIT-6 template and retains the same symmetry after the growth of the Ag shell. High-angle annular dark-field scanning TEM (HAADF-STEM) and the corresponding energy dispersive X-ray spectroscopy (EDS) mapping images of the selected four Meso-Pt@Ag<sub>2</sub> nanocrystals are shown in Figure 2f, where Pt and Ag elements are evenly distributed, indicating that Ag is successfully grown. The corresponding EDS elemental analysis shows that the ratio of Pt to Ag in Meso-Pt@Ag<sub>2</sub> is 84.4% to 15.6% (Figure 2g), while as for Meso-Pt, Meso-Pt@Ag<sub>1</sub>, Meso-Pt@Ag<sub>3</sub>, and Meso-Pt@Ag<sub>4</sub>, the ratios of Pt to Ag are defined as 100.0–0.0%, 90.–9.3%, 77.6–22.4%, and 69.5–30.5%, respectively (Figure S3f, S4f, S5f, S6f, and Table S1, Supporting Information). To better prove the formation of the Ag shell on the Pt core, the EDS line scan elemental profile of one corner of the Meso-Pt@Ag<sub>2</sub> nanocrystal shows that the corresponding element distribution of Ag is more focused on both edges than that of Pt in Figure S7, Supporting Information, which further confirms the core–shell structure of Meso-Pt@Ag<sub>2</sub>.

In addition, the selected area electron diffraction (SAED) pattern confirms that the single Meso-Pt@Ag<sub>2</sub> nanocrystal is polycrystalline. High-resolution TEM (HRTEM) images reveal the lattice spacing of 0.228 nm that belongs to the (111) plane of face-centered cubic (fcc) metallic Pt (Figure 2d). While in Figure S3d, Supporting Information, two lattice spacings of 0.225 and 0.195 nm belong to the (111) and (200) planes of metallic Pt for Meso-Pt, respectively. For Meso-Pt@Ag series, the lattice spacings of Meso-Pt@Ag<sub>1/2/3/4</sub> corresponding to Pt(111) increase successively, which are calculated to be 0.227 nm (Figure S4d, Supporting Information), 0.228 nm (Figure S2d, Supporting Information), 0.229 nm (Figure S5d, Supporting

Information), and 0.231 nm (Figure S6d, Supporting Information), respectively. The lattice spacings of Meso-Pt@Ag nanocrystals are between the (111) plane of Ag (0.235 nm)<sup>[29]</sup> and the (111) plane of Pt (0.225 nm). Therefore, we can deduce that the lattice compression of the Ag shell gradually decreases with the increase in the number of Ag layers, which can combine the lattice strain and the electronic synergy between the core and shell to change the electronic structure of Ag.<sup>[23]</sup> According to X-ray diffraction (XRD) patterns (Figure 2h), all of Meso-Pt@Ag and Meso-Pt nanocrystals exhibit three distinct characteristic peaks at 39.9°, 46.4°, and 67.7° ascribed to (111), (200), and (220) planes of fcc metallic Pt, respectively. Furthermore, in the enlarged XRD patterns, the characteristic peaks of Meso-Pt@Ag have a slight negative shift compared with Meso-Pt, due to the lattice expansion caused by the few-layer Ag wrapped on the Pt surface.<sup>[25]</sup> In the meantime, no characteristic peaks belonging to fcc metallic Ag could be found. Thus, combining with XRD patterns and HRTEM images, we have successfully wrapped Ag shells with different several layers on the Pt core without forming Ag nanocrystals individually.

X-ray photoelectron spectroscopy (XPS) is further utilized to analyze the elemental composition of Meso-Pt@Ag<sub>2</sub> and Meso-Pt nanocrystals, especially the coordination environment of surface atoms. In the full survey spectrum of Meso-Pt@Ag<sub>2</sub> (Figure 3a), there are distinct peaks corresponding to C 1s, Pt 4f, Ag 3d, and Ag MN1. As for Meso-Pt, no peaks belonging to Ag 3d and Ag MN1 can be observed. According to the high-resolution XPS spectra (Figure 3b–d), we conclude that the metallic Pt<sup>0</sup> and Ag<sup>0</sup> are dominant species in the Meso-Pt@Ag<sub>2</sub> and Meso-Pt nanocrystals. For Pt 4f (Figure 3b), two pairs of peaks are assigned to metallic Pt<sup>0</sup> and Pt<sup>2+</sup> species.<sup>[30]</sup> Compared to Meso-Pt, the peaks for Pt 4f of Meso-Pt@Ag<sub>2</sub> show a slight negative shift of 0.14 eV, signing

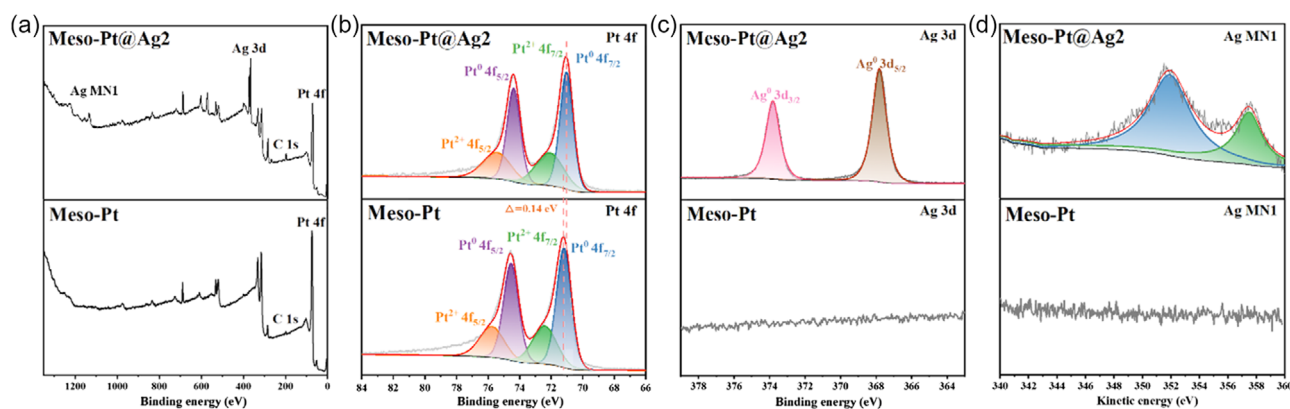


**Figure 3.** XPS survey spectra of Meso-Pt@Ag<sub>2</sub> and Meso-Pt. a) The full survey XPS spectra; and the corresponding high-resolution XPS spectra for b) Pt 4f, c) Ag 3d, and d) Ag MN1 of Meso-Pt@Ag<sub>2</sub> and Meso-Pt, respectively.

that the valence electrons of Ag would be transferred to Pt and the strong charge interaction between the Ag shell and Pt core.<sup>[23]</sup> And, according to XPS spectra for Pt 4f of Meso-Pt, Meso-Pt@Ag<sub>1</sub>, Meso-Pt@Ag<sub>2</sub>, Meso-Pt@Ag<sub>3</sub>, and Meso-Pt@Ag<sub>4</sub> in Figure S8a, Supporting Information, we can also find that the peak position shifts negatively with the increase of the Ag content because more Ag wrapping will transfer more electrons to the Pt core. In addition, two sharp peaks located at 367.8 and 373.8 eV are attributed to Ag<sup>0</sup> 3d<sub>5/2</sub> and 3d<sub>3/2</sub> of Meso-Pt@Ag<sub>2</sub>, respectively (Figure 3c). In the close-up XPS spectra for Ag MN1 of Meso-Pt@Ag<sub>2</sub> (Figure 3d), there are two obvious Auger peaks at around 351.9 and 357.5 eV, which is well consistent with previous reports.<sup>[31]</sup> Combining the spectra for Ag 3d and Ag MN1, the composition of Ag can be confirmed as metallic Ag<sup>0</sup> in Meso-Pt@Ag<sub>2</sub>. Moreover, by observing XPS spectra for Ag 3d of Meso-Pt@Ag<sub>1</sub>, Meso-Pt@Ag<sub>2</sub>, Meso-Pt@Ag<sub>3</sub>, and Meso-Pt@Ag<sub>4</sub> (Figure S8b, Supporting Information), it can be seen that the peak position shifts negatively with the increase of Ag content. This is because the presence of more Ag atoms will transfer fewer electrons from each Ag atom to the Pt core, thus making the binding energy of Ag lower.

### 2.3. Electrocatalytic Properties for Ethanol Oxidation

To investigate the dual effect of the electronic and lattice strain effects in the few-layer Ag shell on their EOR activity, this series of Meso-Pt@Ag catalysts is measured in an alkaline solution. As shown in Figure 4a, the cyclic voltammetry (CV) curves of as-prepared Meso-Pt@Ag, Meso-Pt, and Pt/C are normalized by electrode areas. Among them, Meso-Pt@Ag<sub>2</sub> shows the highest current density of 19.43 mA cm<sup>-2</sup>, which is superior to Meso-Pt@Ag<sub>1</sub> (12.72 mA cm<sup>-2</sup>), Meso-Pt@Ag<sub>3</sub> (11.52 mA cm<sup>-2</sup>), Meso-Pt@Ag<sub>4</sub> (7.73 mA cm<sup>-2</sup>), Meso-Pt (4.83 mA cm<sup>-2</sup>), and commercial Pt/C (2.54 mA cm<sup>-2</sup>). Then, CV curves are further normalized by the Pt mass in Figure 4b in which Meso-Pt@Ag<sub>2</sub> also exhibits the highest mass activities of up to 10.01 A mg<sup>-1</sup><sub>Pt</sub>. In this case, the remarkable mass activity of core-shell Meso-Pt@Ag<sub>2</sub> is 1.59, 1.60, 2.23, 4.45, and 8.40 times that of the core-shell Meso-Pt@Ag<sub>1</sub> (6.27 A mg<sup>-1</sup><sub>Pt</sub>), Meso-Pt@Ag<sub>3</sub> (6.24 A mg<sup>-1</sup><sub>Pt</sub>), Meso-Pt@Ag<sub>4</sub> (4.49 A mg<sup>-1</sup><sub>Pt</sub>) nanocrystals,

pure Meso-Pt (2.25 A mg<sup>-1</sup><sub>Pt</sub>), and Pt/C (1.19 A mg<sup>-1</sup><sub>Pt</sub>), respectively (Figure 4c and Table S2, Supporting Information). Moreover, the calculated  $J_f/J_b$  ratio is used as an important parameter to evaluate the poisoning tolerance to the carbonaceous species for EOR, where  $J_f/J_b$  is the forward/backward current densities.<sup>[32,33]</sup> All core-shell Meso-Pt@Ag nanocrystals show the ratios of  $J_f/J_b > 1$ , while pure Meso-Pt shows a ratio of  $J_f/J_b < 1$ . It indicates that the core-shell structure of the Pt core coated with a few-layer Ag is less poisoned by carbonaceous intermediates compared to the pure Pt surface. In Figure 4d, the corresponding Tafel curves present Meso-Pt@Ag<sub>2</sub> with the lowest slope of 193.6 mV dec<sup>-1</sup>, indicating its optimized charge and mass transfer kinetics.<sup>[34]</sup>

On the other hand, CV curves are recorded in the N<sub>2</sub>-saturated 1.0 M KOH solution (Figure 4e) where two peaks at around 0.05 and 0.27 V represent the H adsorption on the Pt surface for Meso-Pt and Pt/C, respectively. As for core-shell Meso-Pt@Ag nanocrystals, the above two peaks do not appear, but there is an obvious bulge at 0.3–0.9 V, which is because the external Ag inhibits the H adsorption on the Pt surface and the oxidation of the Ag shell, which also proves that the Ag shell wraps the Pt core. Although the hydrogen adsorption method is less reliable to evaluate the electrochemically active surface area (ECSA), the values of these catalysts are roughly estimated by the double-layer capacitance ( $C_{dl}$ ) method (Figure S9, Supporting Information). Among them, Meso-Pt@Ag<sub>2</sub> is 175 μF cm<sup>-2</sup>, which is close to the  $C_{dl}$  of Meso-Pt (206 μF cm<sup>-2</sup>) and Meso-Pt@Ag<sub>1</sub> (191 μF cm<sup>-2</sup>), and larger than that of Meso-Pt@Ag<sub>3</sub> (135 μF cm<sup>-2</sup>) and Meso-Pt@Ag<sub>4</sub> (119 μF cm<sup>-2</sup>) in turn (Figure 4f). This indicates that the excess of reduced Ag in Meso-Pt@Ag<sub>3/4</sub> leads to the partial blockage of the mesopores in Meso-Pt nanocrystals, thereby reducing their ECSA to result in decreased activity. The  $C_{dl}$  of Meso-Pt@Ag<sub>2</sub> is smaller than that of Meso-Pt and Meso-Pt@Ag<sub>1</sub>, but Meso-Pt@Ag<sub>2</sub> exhibits better EOR activity as it owns a suitable Ag shell to change the electronic structure of core-shell Pt@Ag.

Electrochemical impedance spectroscopy (EIS) also reflects the kinetics of EOR. As shown in Figure 4g, the diameter of the semicircle representing the charge transfer resistance ( $R_{ct}$ ) of EOR increases in the order of Meso-Pt@Ag<sub>2</sub>, Meso-Pt@Ag<sub>1</sub>, Meso-Pt@Ag<sub>3</sub>, Meso-Pt@Ag<sub>4</sub>, Meso-Pt, and Pt/C. The

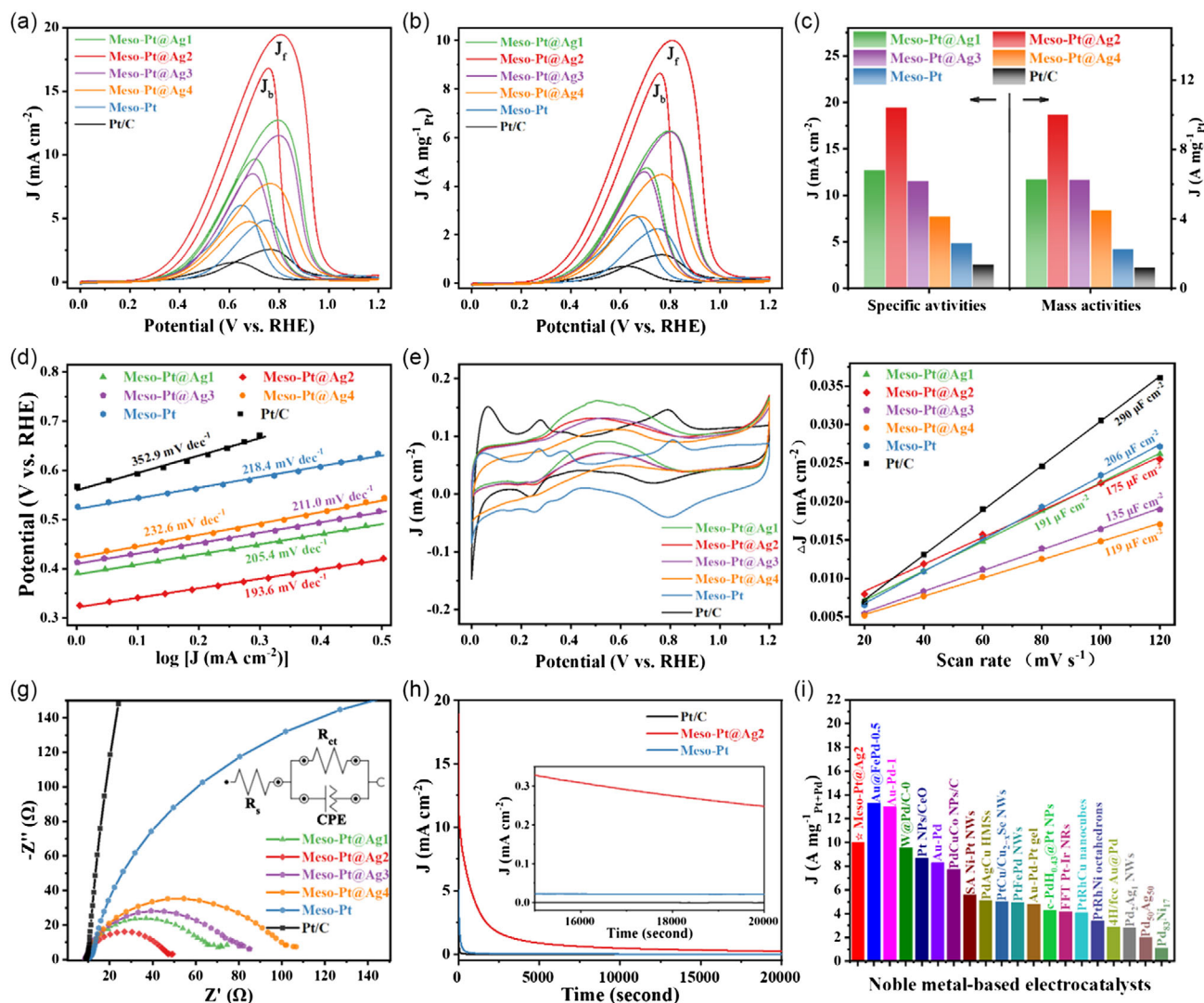


**Figure 4.** Electrochemical EOR performances of various electrocatalysts. CV curves normalized by a) electrode areas, b) Pt mass; c) the comparison of specific activities and mass activities; d) the corresponding Tafel slopes, e) CV curves in  $\text{N}_2$ -saturated 1.0 M KOH solution; f) capacitive currents at 0.40 V versus RHE with various scan rates; g) EIS Nyquist plots and the corresponding equivalence circuit; h) chronoamperometric curves; i) the activity comparison of core-shell Meso-Pt@Ag<sub>2</sub> nanocrystals with recently reported Pt/Pd-based nanocatalysts.

minimum semicircle diameter of the Meso-Pt@Ag<sub>2</sub> means the smallest  $R_{\text{ct}}$ , which indicates that the Ag shell wrapping the Pt core accelerates the charge transfer during ethanol oxidation and optimizes the reaction kinetics. This is also in accord with the obtained Tafel slope.<sup>[35]</sup> Furthermore, after continuous chronoamperometry for 20 000 s, Meso-Pt@Ag<sub>2</sub> exhibits the slowest current density decay, which is sequentially better than that of Meso-Pt and Pt/C, indicating its excellent electrocatalytic durability and antitoxicity (Figure 4h). Meanwhile, we also use the accelerated test to evaluate the EOR stability of Meso-Pt@Ag<sub>2</sub>. After 200 cycles of CV tests, Meso-Pt@Ag<sub>2</sub> can still retain 94.8% of the peak current density (Figure S10, Supporting Information). In addition, it is worth mentioning that the mass activity of our optimized core-shell Meso-Pt@Ag<sub>2</sub> is superior to the vast majority of previously reported catalysts (Figure 4i and Table S3, Supporting Information).

#### 2.4. Meso-Pt@Ag<sub>2</sub> Nanocrystals After the EOR Reaction

In order to confirm the stability of Meso-Pt@Ag<sub>2</sub> nanocrystals after the EOR reaction for 20 000 s, we have carried out morphology and structure characterization of Meso-Pt@Ag<sub>2</sub> after EOR. As shown in Figure S11, Supporting Information, it can be seen from the SEM and TEM images of Meso-Pt@Ag<sub>2</sub> after EOR that the morphology and pore structure remain almost unchanged. In the HRTEM image (Figure S11d, Supporting Information), the lattice fringes of 0.228 nm belong to the (111) plane of Pt, and the lattice fringes of 0.235 nm belong to the (111) plane of the Ag shell. This indicates that the structure of Meso-Pt@Ag<sub>2</sub> hardly changes after EOR, and the Ag shell keeps in the outer layer of the Pt core. Furthermore, the composition of Pt and Ag elements of Meso-Pt@Ag<sub>2</sub> basically does not change after the reaction (Figure S11e-f, Supporting Information).

Accordingly, we can find that the structure of Meso-Pt@Ag<sub>2</sub> remains stable after the EOR reaction.

## 2.5. In Situ Raman Spectra and Density Functional Theory Calculations

By in situ Raman spectra and density functional theory (DFT) calculations, the surface reaction mechanism of EOR can be further probed. **Figure 5a,b** shows the in situ Raman spectra from 0.0 to 1.0 V versus RHE of Meso-Pt@Ag<sub>2</sub> and Meso-Pt nanocrystals, respectively. The peaks at 878, 1044, and 1446 cm<sup>-1</sup> corresponding to C–C–O, & as (CH<sub>3</sub>), and ω(CH<sub>2</sub>) of CH<sub>3</sub>CH<sub>2</sub>OH are gradually weakened with the increase of the applied voltage, indicating the consumption of CH<sub>3</sub>CH<sub>2</sub>OH during the EOR process.<sup>[36]</sup> Furthermore, the peaks assigned to ρ(CH<sub>3</sub>) and τω(CH<sub>2</sub>) at 1090 and 1268 cm<sup>-1</sup> decay because of the deprotonation of CH<sub>3</sub>CH<sub>2</sub>OH during electrooxidation.<sup>[36]</sup> While as the EOR proceeds, CH<sub>3</sub>CH<sub>2</sub>OH is completely oxidized to more CO<sub>2</sub> molecules and converted to HCO<sub>3</sub><sup>-</sup> in KOH solution, which resulted in the enhancement of the peak at 1065 cm<sup>-1</sup> corresponding to HCO<sub>3</sub><sup>-</sup>.<sup>[37]</sup> Thus, it could be reasonably concluded that the CH<sub>3</sub>CH<sub>2</sub>OH molecules adsorbed on the Meso-Pt@Ag<sub>2</sub> and Meso-Pt surfaces undergo a process of deprotonation and are finally converted into CO<sub>2</sub>.

Next, the Pt (111) model to represent the pure Meso-Pt, the 1-layer Ag-coated Pt (Pt@1 L-Ag (111)) model, and the 2-layer Ag-coated Pt (Pt@2 L-Ag (111)) model to represent few-layer Ag-coated Meso-Pt are constructed to analyze the effect of the

electronic effect and strain effect between the Ag shell and the Pt core for EOR (Figure 5c). We have calculated the important deprotonation process during ethanol oxidation of Pt(111), Pt@1L-Ag (111), and Pt@2L-Ag (111) models.<sup>[38]</sup> The calculated Gibbs free energy for the deprotonation process of the first four protons is shown in Figure 5d. The rate-determining step (RDS) of deprotonation on Pt (111) surface is the step IV CH<sub>3</sub>–\*CO → \*CH<sub>2</sub>–CO + H<sup>+</sup> + e<sup>-</sup> with ΔG<sub>4</sub> of 1.22 eV. Then, with the Ag coating, the RDS of Pt@1 L-Ag (111) surface becomes the step I CH<sub>3</sub>–CH<sub>2</sub>OH → CH<sub>3</sub>–\*CHOH + H<sup>+</sup> + e<sup>-</sup> with ΔG<sub>1</sub> of 0.97 eV, which is smaller than Pt@2L-Ag (111) surface of ΔG<sub>1</sub> of 1.05 eV and Pt (111) surface of ΔG<sub>4</sub> of 1.22 eV (Figure 5d). This suggests that the Ag coating on the Pt core promotes the reaction kinetics of ethanol deprotonation. Furthermore, the adsorption between the CO and the catalyst has a significant effect on the catalytic efficiency and anti-toxicity of the catalyst. Here, projected electronic densities of states (PDOS) of adsorbed metal atoms in surfaces, the CO molecules, and their interaction within adsorbed metal atom-CO configurations are exhibited in Figure 5e, Figure S12, Supporting Information. As the number of layers of wrapped Ag increases on the Pt(111) surface, d<sub>π\*</sub> orbitals obtained by hybridization of the p orbitals of CO and the d orbitals of the adsorbed metal atom gradually close to the Fermi level.<sup>[39]</sup> And, the d-band centers of Pt in Pt(111) (-2.59 eV), Ag in Pt@1L-Ag(111) (-3.91 eV), and Ag in Pt@2L-Ag(111) (-4.58 eV) shift down sequentially, indicating that the encapsulation of Ag weakens the binding energy between CO and adsorption sites (Figure S12, Supporting Information). In addition, CO exhibits a strong adsorption on

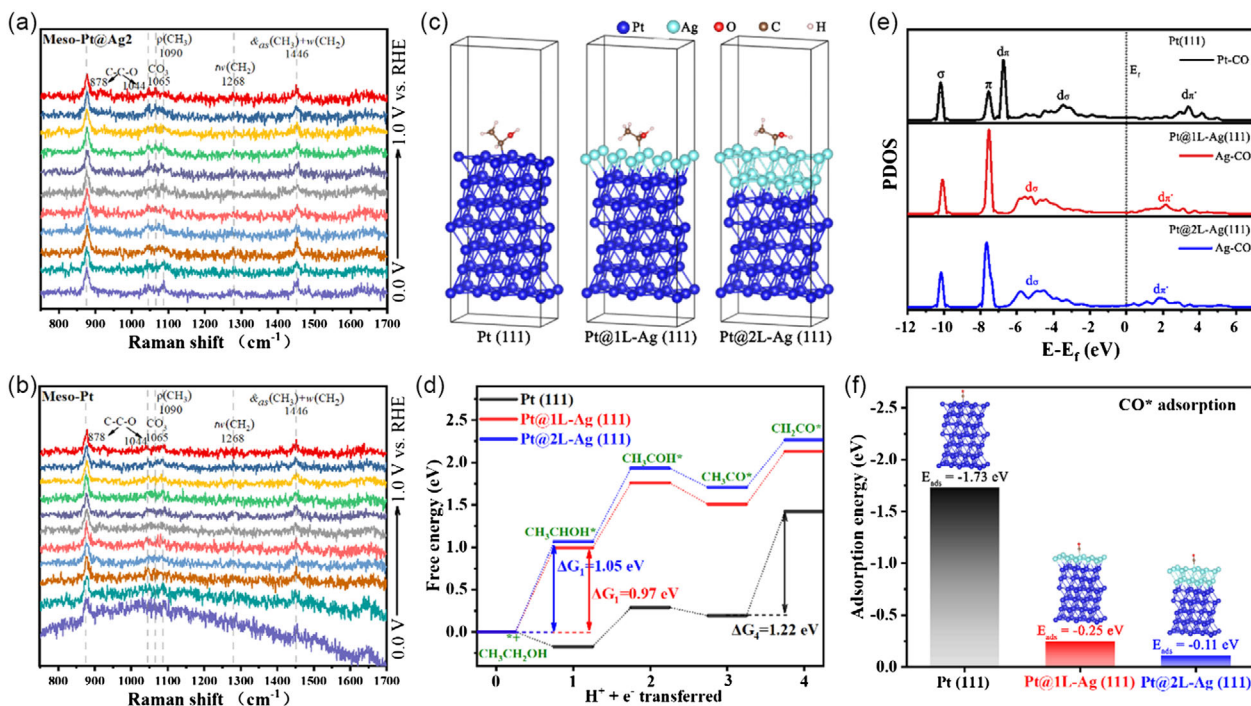


**Figure 5.** In situ Raman spectra and DFT calculations. In situ Raman spectra of a) Meso-Pt@Ag<sub>2</sub> and b) Meso-Pt nanocrystals; c) the adsorption configuration of CH<sub>3</sub>CH<sub>2</sub>OH and d) reaction energy profile of intermediates for ethanol oxidation on Pt (111), Pt@1L-Ag (111), and Pt@<sub>2</sub>L-Ag (111) models; e) PDOS profiles of metal-CO configuration in various models; f) adsorption energies of CO on Pt (111), Pt@1 L-Ag (111), and Pt@<sub>2</sub>L-Ag (111) surfaces.

the Pt (111) surface with an adsorption energy ( $E_{\text{ads}}$ ) of  $-1.73$  eV, while the  $E_{\text{ads}}$  of CO on the Ag-coated Pt (111) surface is much reduced where the  $E_{\text{ads}}$  of CO on the Pt@2L-Ag (111) surface is  $-0.11$  eV, smaller than that of Pt@1L-Ag (111) of  $-0.25$  eV (Figure 5f). Therefore, it is verified that the Ag-coated Pt surface performs more optimized surface conditions for CO stripping compared to the pure Pt surface, which helps to improve the CO antitoxicity and the EOR efficiency of the electrocatalyst.

### 3. Conclusions

To sum up, we have developed a strategy to synthesize a series of few-layer Ag-coated ordered mesoporous Pt nanocrystals with different Ag shell thicknesses by combining hard templating and in situ reduction. The ordered mesoporous structure provides high specific surface area and fast mass transfer channels. The synergistic electronic and lattice strain effects induced by the few-layer Ag-coated core-shell structure can optimize the electronic structure of Ag atoms on the surface. Due to the advantages brought by the ordered mesoporous structure and the few-layer Ag-coated core-shell structure, Meso-Pt@Ag<sub>2</sub> exhibits the highest mass activity of  $10.01 \text{ A mg}_{\text{Pt}}^{-1}$  in the alkaline electrolyte, respectively, 8.4 times and 4.45 times that of commercial Pt/C and pure Meso-Pt. Meanwhile, Meso-Pt@Ag<sub>2</sub> also performs the higher toxicity resistance to carbonaceous intermediates and stability. Furthermore, theoretical calculations also suggest that Ag atoms on the surface of the Pt(111) slab have more optimized deprotonation reaction kinetics and lower CO adsorption energy, signing that it has stronger resistance to CO toxicity. This study provides an effective idea for precisely designing hierarchical core-shell porous catalysts and utilizing the electronic synergy and lattice strain effect between the core and shell to optimize the electronic structure of the catalyst surface for efficient catalytic reactions.

### 4. Experimental Section

**Synthesis of Meso-Pt@Ag<sub>2</sub>, Meso-Pt@Ag<sub>1</sub>, Meso-Pt@Ag<sub>3</sub>, and Meso-Pt@Ag<sub>4</sub> Nanocrystals:** The detailed synthesis steps for the precursor of Meso-Pt nanocrystals are shown in the Supporting Information. The yield of Meso-Pt nanocrystals is 97%. Then, the above 5 mL of  $1 \text{ mg Pt mL}^{-1}$  suspension of Meso-Pt nanocrystals is diluted to 25 mL of  $0.2 \text{ mg Pt mL}^{-1}$  suspension. Then, pure hydrogen gas with a flow rate of  $200 \text{ mL min}^{-1}$  is bubbled through the diluted suspension for 1 h to absorb H<sub>2</sub> on the Pt surface. The obtained black nanocrystals are denoted as Meso-Pt@PtH<sub>x</sub>. The above 5 mL suspension ( $0.2 \text{ mg Meso-Pt@PtH}_x/1 \text{ mL H}_2\text{O}$ ) is placed in a glass bottle with a stirring speed of 1200 rpm. Then, 1 mL of  $1.50 \text{ mg mL}^{-1}$  AgNO<sub>3</sub> solution is slowly injected into it with a flow rate of  $0.025 \text{ mL min}^{-1}$ . After the Ag reduction for 1 h, the reacted suspension is centrifuged and washed with water three times, and the collected nanocrystals are dispersed in H<sub>2</sub>O named Meso-Pt@Ag<sub>2</sub>. Similarly, Meso-Pt@Ag<sub>1</sub>, Meso-Pt@Ag<sub>3</sub>, and Meso-Pt@Ag<sub>4</sub> could be successfully obtained by changing the concentration of AgNO<sub>3</sub> solution by 0.75, 2.25, and  $3.00 \text{ mg mL}^{-1}$ , respectively. In the above steps of synthesizing Meso-Pt@PtH<sub>x</sub> and Meso-Pt@Ag, almost no material is lost during transfer and centrifugation, and the yields of Meso-Pt@Ag nanocrystals are close to 100%.

### Supporting Information

Supporting Information is available from the Wiley Online Library or from the author.

### Acknowledgements

This work was financially supported by the Guangdong Natural Science Funds for Distinguished Young Scholar (grant no. 2018B030306050) and the National Natural Science Foundation of China (grant nos. 21601137, 22105147, 22138003, and 21825802).

### Conflict of Interest

The authors declare no conflict of interest.

### Data Availability Statement

The data that support the findings of this study are available from the corresponding author upon reasonable request.

### Keywords

core-shell nanostructures, ethanol oxidation, molecular sieves, ordered mesopores, Pt@Ag nanocrystals

Received: January 8, 2023

Revised: March 6, 2023

Published online: March 22, 2023

- [1] Z. Xia, S. Guo, *Chem. Soc. Rev.* **2019**, *48*, 3265.
- [2] X. Wang, L. Chai, J. Ding, L. Zhong, Y. Du, T.-T. Li, Y. Hu, J. Qian, S. Huang, *Nano Energy* **2019**, *62*, 745.
- [3] Q. Huang, Y. Guo, D. Chen, L. Zhang, T.-T. Li, Y. Hu, J. Qian, S. Huang, *Chem. Eng. J.* **2021**, *424*, 130336.
- [4] Y. Zhang, B. Chen, D. Guan, M. Xu, R. Ran, M. Ni, W. Zhou, R. O'Hayre, Z. Shao, *Nature* **2021**, *591*, 246.
- [5] K. Kodama, T. Nagai, A. Kuwaki, R. Jinnouchi, Y. Morimoto, *Nat. Nanotechnol.* **2021**, *16*, 140.
- [6] G. Liu, W. Zhou, Y. Ji, B. Chen, G. Fu, Q. Yun, S. Chen, Y. Lin, P. F. Yin, X. Cui, J. Liu, F. Meng, Q. Zhang, L. Song, L. Gu, H. Zhang, J. Am. Chem. Soc. **2021**, *143*, 11262.
- [7] X. Zhao, Q. Liu, Q. Li, L. Chen, L. Mao, H. Wang, S. Chen, *Chem. Eng. J.* **2020**, *400*, 125744.
- [8] C. W. Anson, S. S. Stahl, *Chem. Rev.* **2020**, *120*, 3749.
- [9] J. Zhang, S. Lu, Y. Xiang, S. P. Jiang, *ChemSusChem* **2020**, *13*, 2484.
- [10] Z. Liang, L. Song, S. Deng, Y. Zhu, E. Stavitski, R. R. Adzic, J. Chen, J. X. Wang, *J. Am. Chem. Soc.* **2019**, *141*, 9629.
- [11] Y. Zhu, L. Bu, Q. Shao, X. Huang, *ACS Catal.* **2019**, *9*, 6607.
- [12] X. Yu, J. Liu, J. Li, Z. Luo, Y. Zuo, C. Xing, J. Llorca, D. Nasiatou, J. Arbiol, K. Pan, T. Kleinhanns, Y. Xie, A. Cabot, *Nano Energy* **2020**, *77*, 105116.
- [13] Y. Zhu, L. Bu, Q. Shao, X. Huang, *ACS Catal.* **2020**, *10*, 3455.
- [14] X. Yu, Z. Luo, T. Zhang, P. Tang, J. Li, X. Wang, J. Llorca, J. Arbiol, J. Liu, A. Cabot, *Chem. Mater.* **2020**, *32*, 2044.
- [15] M. B. Gawande, A. Goswami, T. Asefa, H. Guo, A. V. Biradar, D. L. Peng, R. Zboril, R. S. Varma, *Chem. Soc. Rev.* **2015**, *44*, 7540.
- [16] H. Chen, K. Shen, Q. Mao, J. Chen, Y. Li, *ACS Catal.* **2018**, *8*, 1417.
- [17] S. Gong, Y.-X. Zhang, Z. Niu, *ACS Catal.* **2020**, *10*, 10886.

- [18] X. Wang, Z. Ma, L. Chai, L. Xu, Z. Zhu, Y. Hu, J. Qian, S. Huang, *Carbon* **2019**, *141*, 643.
- [19] J. R. Kitchin, J. K. Nørskov, M. A. Barteau, J. G. Chen, *Phys. Rev. Lett.* **2004**, *93*, 156801.
- [20] J. R. Kitchin, J. K. Nørskov, M. A. Barteau, J. G. Chen, *J. Chem. Phys.* **2004**, *120*, 10240.
- [21] P. Strasser, S. Koh, T. Anniyev, J. Greeley, K. More, C. Yu, Z. Liu, S. Kaya, D. Nordlund, H. Ogasawara, M. F. Toney, A. Nilsson, *Nat. Chem.* **2010**, *2*, 454.
- [22] L. Bu, N. Zhang, S. Guo, X. Zhang, J. Li, J. Yao, T. Wu, G. Lu, J.-Y. Ma, D. Su, X. Huang, *Science* **2016**, *354*, 1410.
- [23] E. Fidiani, G. Thirunavukkarasu, Y. Li, Y.-L. Chiu, S. Du, *J. Mater. Chem. A* **2020**, *8*, 11874.
- [24] J. Deng, P. Ren, D. Deng, X. Bao, *Angew. Chem. Int. Ed.* **2015**, *54*, 2100.
- [25] M. Qiao, H. Wu, F. Y. Meng, Z. Zhuang, J. X. Wang, *Small* **2022**, *18*, 2106643.
- [26] H. Wang, H. Y. Jeong, M. Imura, L. Wang, L. Radhakrishnan, N. Fujita, T. Castle, O. Terasaki, Y. Yamauchi, *J. Am. Chem. Soc.* **2011**, *133*, 14526.
- [27] L. Chen, B. Huang, X. Qiu, X. Wang, R. Luque, Y. Li, *Chem. Sci.* **2016**, *7*, 228.
- [28] H. Lv, D. Xu, C. Kong, Z. Liang, H. Zheng, Z. Huang, B. Liu, *ACS Cent. Sci.* **2020**, *6*, 2347.
- [29] M. Madasu, P. L. Hsieh, Y. J. Chen, M. H. Huang, *ACS Appl. Mater. Interfaces* **2019**, *11*, 38039.
- [30] Y. Zhang, F. Gao, P. Song, J. Wang, J. Guo, Y. Shiraishi, Y. Du, *ACS Sustain. Chem. Eng.* **2019**, *7*, 3176.
- [31] H. Wang, Y. Yu, S. You, J. Meng, M. Muska, Q. Li, Q. Yang, *Adv. Opt. Mater.* **2021**, *9*, 2002080.
- [32] R. Du, J. Wang, Y. Wang, R. Hubner, X. Fan, I. Senkovska, Y. Hu, S. Kaskel, A. Eychmuller, *Nat. Commun.* **2020**, *11*, 1590.
- [33] M. S. Ahmed, S. Jeon, *ACS Catal.* **2014**, *4*, 1830.
- [34] H. Peng, J. Ren, Y. Wang, Y. Xiong, Q. Wang, Q. Li, X. Zhao, L. Zhan, L. Zheng, Y. Tang, Y. Lei, *Nano Energy* **2021**, *88*, 106307.
- [35] D. Liu, Q. Zeng, H. Liu, C. Hu, D. Chen, L. Xu, J. Yang, *Cell Rep. Phys. Sci.* **2021**, *2*, 100357.
- [36] W. Zhang, S. T. Oyama, *J. Phys. Chem.* **1996**, *100*, 10759.
- [37] P. A. G. L. Samarakoon, N. H. Andersen, C. Perinu, K.-J. Jens, *Energy Proc.* **2013**, *37*, 2002.
- [38] E. D. Wang, J. B. Xu, T. S. Zhao, *J. Phys. Chem. C* **2010**, *114*, 10489.
- [39] N. Dimakis, M. Cowan, G. Hanson, E. S. Smotkin, *J. Phys. Chem. C* **2009**, *113*, 18730.